arXiv:1512.05527v1 [physics.flu-dyn] 17 Dec 2015

Turbulent separation in a channel with a curved wall

J.-P. MOLLICONE, F. BATTISTA, P. GUALTIERI AND C.M. CASCIOLA †

Department of Mechanical and Aerospace Engineering, Sapienza University of Rome, via Eudossiana 18, 00184 Rome, Italy

(Received ?; revised ?; accepted ?. - To be entered by editorial office)

Flow separation, in both external and internal flows, is the main source of turbulent fluctuations which ultimately results in drag and inefficiency in applications. The basic issue of turbulence self sustainment is still not exhaustively investigated for even mildly complex geometries able to induce separation. In order to provide insightful information on the origin of form drag and related turbulent kinetic energy production and dissipation mechanisms, Direct Numerical Simulations (DNS) of turbulent channel flows with a bump at one of the walls are discussed. The shape of the bump is modified to address the effect of the bluffness on the dynamics of the separation bubble behind the bump. Global quantities reveal that most of the drag is due to the form contribution, whilst the friction contribution does not change appreciably with respect to an equivalent planar channel flow. Beside turbulent kinetic energy, the geometrical complexity of the flow requires the explicit analysis of the energy budget for the mean flow. The energy introduced by the pressure drop follows two routes: part of it is transferred towards the walls to be dissipated and part feeds the turbulent production in the separating shear layer. Apart from being dissipated, the turbulent kinetic energy is spatially redistributed by the turbulent fluxes to sustain fluctuations in the bulk of the flow and within the bubble. The present results shed light on the intermingled processes of production, transfer and dissipation of energy in complex turbulent flows where a crucial role is played by the flux terms that move the energy from places where it is generated to the locations where most dissipation occurs.

Key words: Recirculation Bubble, Form Drag, Turbulent Kinetic Energy Fluxes, Direct Numerical Simulation, Bluff Body, Channel flow

1. Introduction

Flow separation consists of fluid flow around bodies becoming detached, causing the fluid closest to the object's surface to flow in reverse or different directions, most often giving rise to turbulent flow. Often the flow Reynolds number is extremely high, e.g. separation around vehicles, but there are cases where moderate Reynolds numbers are achieved, e.g. when separation occurs behind an arterial stenosis. Sometimes flow separation is induced by geometrical singularities, like in presence of sharp corners. In other cases the geometry varies smoothly, but the resulting adverse pressure gradient is sufficient for flow detachment. Given its importance both from a theoretical and a practical point of view, the study of turbulence and separation has long been of interest to the fluid mechanics community, see e.g. Simpson (1989) for a review. However, due to its

† Email address for correspondence: carlomassimo.casciola@uniroma1.it

complexity, this classic subject is still incompletely explored in turbulent conditions. The separation of fluid flow from objects inevitably results in effects such as increased drag and mixing, momentum and energy transfer and vortex shedding. For example, an understanding of such effects is helpful to improve road vehicle performances, in the study of fluid-structure interactions, to regulate air mixing with other substances (e.g. pollutants or fuels), in the study of boundary layer control, see e.g. Marusic *et al.* (2014) and Bai *et al.* (2014), and in modern bioengineering applications such as in hemodynamics, where a decrease in blood vessel section induced by the local degeneration of the arterial wall (atherosclerosis) may lead to boundary layer separation phenomena.

Turbulent boundary layers with pressure gradients are a common characteristic of many aerodynamic flows, e.g. the flow past airfoils, gas turbine blades, sails and diffusers. Many researchers investigated such flows in conditions characterised by an incipient or complete separation. To correctly predict the behaviour and the efficiency of airfoils or wings, the understanding of the separation and reattachment mechanisms is essential. Nonetheless the fundamental mechanisms are far from being completely understood and no entirely satisfactory turbulence models for numerical simulation of high Reynolds number separated flows are nowadays available. The reasons mainly resides in the complexity of the geometries inducing the separation and in the fact that both experimental and numerical data are not sufficiently accurate to allow a reliable statistical analysis.

In external flows, boundary layer separation is induced by a strong adverse pressure gradient (APG) and is considered one of the most challenging issues in fluid dynamics, see e.g. Wilcox (1993). In these conditions, the classical scaling of turbulent statistics is not valid since the flow separation modifies the Reynolds shear stress distribution, see e.g. Skaare & Krogstad (1994). Flow separation may also take place in internal flows, like the turbulent channel flow or the pipe flow, where, on average, the pressure decreases in the flow direction. There, as a consequence of an abrupt change of the local section, the pressure gradient may locally revert producing localised separation in the form of a statistically steady recirculation behind the region of reduced area, e.g. caused by a bump in the wall. Under many respects, this could be considered as an ideal configuration for the study of flow separations, especially when the flow is fully turbulent. Statistical stationarity allows to acquire sufficient statistics to address the basic issue of turbulence sustainment in the separation bubble and, in the case of an isolated bump in an otherwise constant section duct, a well characterised and understood turbulent state is expected to be recovered sufficiently upstream and downstream of the obstacle. In fact, the issue of statistical accuracy is crucial in the study of inhomogeneous flows, where all the symmetries compatible with the phenomenology of interest provide the invaluable opportunity to increase the statistics. In the present case, homogeneity in the normal direction is inevitably broken by the wall and streamwise homogeneity is violated by the obstacle itself. The remaining symmetries, i.e. homogeneity in time and in the transverse direction, should then be exploited. These basic considerations lead to consider the flow in a channel with a huge transverse extension (ideally, infinite width) and parallel planar walls except for an isolated bump in one of the two walls as the ideal flow configuration to address basic issues concerning flow separation.

Most of our knowledge concerning separated flows has been obtained experimentally by using hot wire anemometry. The experimental generation of turbulent flow with adverse pressure gradient is not standardised and the different approaches employed so far lead to substantially different configurations where the control on the actual pressure gradient and on the ensuing separated flow is limited. Skaare & Krogstad (1994) and Krogstad & Skaare (1995) performed a detailed study of a turbulent boundary layer in presence of a strong APG and constant skin friction coefficient, providing a

detailed analysis of the turbulence statistics including the budget of the kinetic energy. In Webster *et al.* (1996) the experimental data of an APG boundary layer created by a bump in the wall are provided and a detailed analysis of the turbulence statistics is discussed. Dengel & Fernholz (1990) performed experimental measurements of APG turbulent boundary layer reporting different cases of pressure distributions, with and without reverse flow. The strong dependence of the near-wall flow properties on the presence or absence of the recirculation region was discussed in detail. These different studies provide a useful description of the velocity fluctuation in the near wall region even though the access to complete flow field data is still limited in experiments. In such cases, numerical simulations can provide invaluable complementary information.

Among the methods employed in numerics to introduce an APG, one of the easiest ways is to exploit wall flow suction. Alternatively, the APG can be prescribed by a body force. Na & Moin (1998*a*) and Na & Moin (1998*b*) performed a DNS of separated boundary layer on a flat plate using a suction/blowing velocity distribution at the upper wall. The inflow condition was taken from Spalart's temporally evolving zero pressure gradient (ZPG) simulation. Chong *et al.* (1998) used the data from the DNS of Na and Moin and from the ZPG DNS of Spalart, see Spalart (1988), to analyse the topology of near-wall coherent structures using the invariants of the velocity gradient tensor. The comparison of experimental and DNS data is presented in Spalart & Watmuff (1993) for turbulent boundary layers with different pressure gradients. The DNS was performed using a spectral code with a fringe region to deal with periodic conditions in the non-homogeneous streamwise direction and the friction velocity at the edge of the boundary layer was prescribed to reproduce the pressure gradient of the experiment. More recently, Skote & Henningson (2002) performed the DNS of separated boundary layer flow with two different adverse pressure gradients, while Ohlsson *et al.* (2010) addressed the separation in a three dimensional turbulent diffuser.

Alternatively, flow separation can be induced by curved walls. Some recent simulations have been conducted with finite differences or finite volume codes which are usually less accurate with respect to spectral codes. Issues related to the separation control have been investigated by Neumann & Wengle (2004), by mean of Large Eddy Simulations (LES). However the sub-grid scale models needed in any LES are expected to hamper the physical understanding of the turbulence dynamics at the smallest scales, calling for the use of DNS where no modelling assumptions are introduced. The LES performed by Wu & Squires (1998) was compared to the results by Webster *et al.* (1996) and it emerged that the use of a coarse resolution with an eddy viscosity model did not allow an accurate description of the small coherent vortical structures in the near wall region which were observed in experiments.

The aim of the present paper is to study flow separation induced in a channel by a lower curved wall forming a bump with varying aspect ratios. The basic issue of turbulence sustainment, which is well understood for canonical wall bounded flows, is still not exhaustively investigated for even mildly complex geometries able to induce separation such as lower curved walls. Only a few simulations are available, see e.g. Marquillie *et al.* (2008) where a similar but smoother profile with different boundary conditions is addressed. Indeed, the DNS performed by Marquillie et al., see Marquillie & Ehrenstein (2003) and Marquillie *et al.* (2008), represents an important contribution towards the understanding of separated flows. The main outcomes show intense vortical structures in correspondence of the separation bubble on the lower wall and also on the upper flat wall where separation does not occur. In addition, turbulent kinetic energy budgets show how energy production and dissipation significantly increase downstream after the lower curved wall up to the reattachment point.

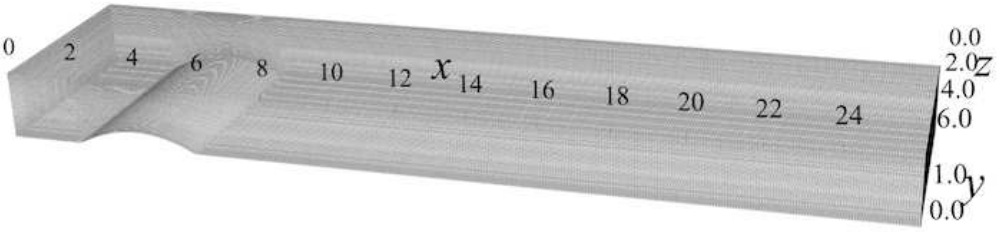

Figure 1: Sketch of the geometry of the channel with the curved lower wall for simulation (A). Periodic conditions are enforced in the streamwise, x, and spanwise, z, direction.

The simulations presented in the present paper intend to investigate, through DNS, the correlation between separation phenomena and localisation of TKE production, transport and dissipation for different lower curved wall geometries, thereby addressing basic issues concerning turbulence production and self-sustainment in the separation bubble and their dependence on the geometrical parameters. The simulations to be discussed are performed using the spectral element method as implemented in the Nek5000 code, see Fischer *et al.* (2008), which allowed for efficient runs on highly parallel architectures.

Section § 2 deals with the methodology and the parameters employed to perform the DNS. Section § 3 starts with the qualitative analysis of the flow features by visualising the instantaneous velocity and vorticity fields and proceeds with the statistical analysis of the flow. Finally § 4 summarizes the main results of the paper and draws the main conclusions.

2. Methodology and Equations

DNS is employed to solve the incompressible Navier-Stokes equations,

$$\frac{\partial u_i}{\partial t} + u_j \frac{\partial u_i}{\partial x_j} = -\frac{\partial p}{\partial x_i} + \frac{1}{Re}\frac{\partial^2 u_i}{\partial x_j^2} \qquad \frac{\partial u_i}{\partial x_i} = 0, \tag{2.1}$$

where u_i is the i^{th} velocity component, and p is the hydrodynamic pressure. $Re = h_0 U_b/\nu$ is the Reynolds number, where h_0 is half the nominal channel height, U_b is the bulk velocity and ν is the kinematic viscosity. For the sake of definiteness, all length scales are made dimensionless with the nominal channel half-height, h_0, time with h_0/U_b and pressures with ρU_b^2. When needed, the adoption of wall units will be explicitly stressed by the customary superscript $+$. Where convenient, the index $i = 1, 2, 3$ will be replaced with the corresponding label, x, y or z, with x the streamwise and z the spanwise coordinate, respectively. The CFD solver used is Nek5000, see Fischer *et al.* (2008), which is based on the spectral element method (SEM), see Patera (1984). The SEM is similar to the finite element method but uses high degree polynomials in each element. The simulations require well-refined grids to capture the turbulence dynamics at all physically relevant length-scales especially in the near wall region and therefore entail large memory and computational power requirements.

Figure 1 shows a sketch of one of the simulated geometries of a channel with a curved lower wall, also referred to as "bump". The domain has dimensions $(L_x \times L_y \times L_z) = (26 \times 2 \times 2\pi)$. Flow is from left to right in the x direction with periodic boundary conditions in both the streamwise and spanwise directions. No slip boundary conditions are imposed at the top and bottom walls. The total channel length is sufficient, compared to the

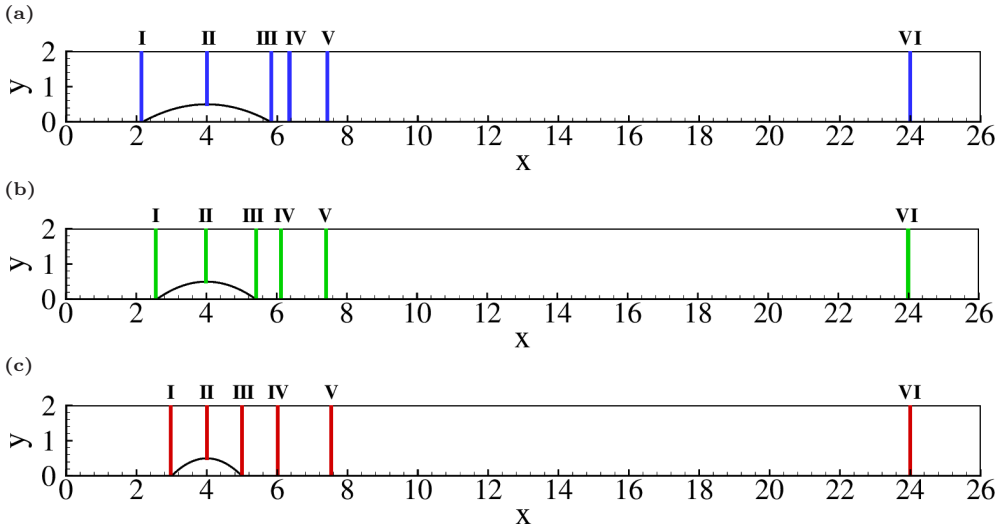

Figure 2: Two dimensional sketches of the channels simulated with different lower curved wall geometries. From top to bottom: simulation (A) - characterised by a streamlined bump, simulation (B) - a bump with a smaller streamwise dimension compared to (A) and simulation (C) - the smallest streamwise dimension of the bump. The bump height is kept constant. The coloured vertical stations correspond to the locations of the profiles to be discussed later.

bump width, to allow the flow to stabilise downstream, recovering the typical turbulent channel flow behaviour before re-entering the domain upstream due to periodicity. Even if such a long channel is computationally expensive, this avoids the use of synthetic inflow conditions or coupling with a separate channel simulation and allows for more realistic incoming turbulent flow conditions. The flow is sustained by means of an overall pressure drop across the channel length $\Delta p(t)$ that is modulated in time to keep the flow rate constant. For the different geometries Δp is adjusted to always have the same mass flux.

The setup is used to study the way the flow changes between the separated region after the bump to the stabilised, channel-like flow downstream. The bulk Reynolds number based on half the channel height is $Re_b = 2500$, with a maximum local friction Reynolds number $Re_\tau = h(x)u_\tau(x)/\nu \simeq 250$, where $u_\tau = \sqrt{\tau_w/\rho}$ with $\tau_w(x)$ the local average shear stress and $h(x)$ half the local channel height. It is worthwhile to note that, due to the unconventional shape of the domain, Re_τ is not constant along the streamwise direction. The nominal friction Reynolds number, defined as Re_τ evaluated where the planar channel flow behaviour is recovered, is $Re_\tau^0 = 175$. This detail is highlighted and discussed in § 3. Three different geometries have been simulated, labelled as (A), (B) and (C). These geometries differ in the shape of the bump, going from a streamlined shape, case (A), towards a more bluff shape, case (C). Figure 2 shows the 2D shapes of the bumps in the xy-plane (the z direction is homogenous) of the domain and highlights six streamwise stations where statistical quantities are evaluated. From left to right, the stations correspond to the bump leading edge (I), top (II) and trailing edge (III), the middle (IV) and the end (V) of the separation bubble and the station at which the channel-like behaviour is recovered (VI). The simulations have been carried out on a BLUE-GENE/Q machine and required an average of 3.5 million core hours

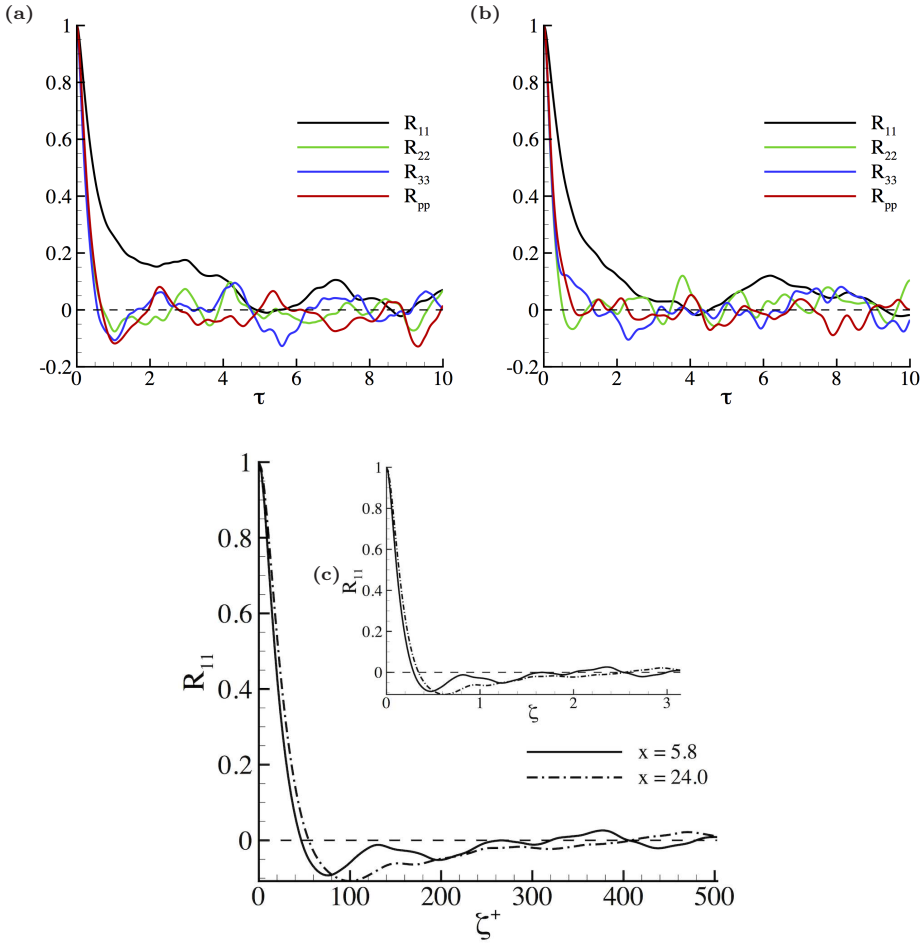

Figure 3: Top panels: temporal auto-correlation of velocity and pressure signals probed just after the bump at $x = 5.8$ (a) and in the channel-like region at at $x = 24.0$ (b). Bottom panel: spatial correlation of axial velocity fluctuations in the spanwise direction at $x = 5.8$ and at $x = 24.0$. All panels refer to the same distance from the upper planar wall, $d = 2 - y = 1.6$.

per simulation. Approximately 400 completely statistically uncorrelated fields, separated by a time interval of $\Delta t_{stat} = 6$, are collected in order to obtain properly converging statistics. Figure 3 reports the temporal auto-correlation of velocity,

$$R_{ii}(x,y,\tau) = \lim_{T\to\infty} \frac{1}{\pi T u_{i_{\rm rms}}^2} \int_0^T \int_0^\pi u_i'(x,y,z,t) u_i'(x,y,x,t+\tau) dz dt$$
$$= \frac{\langle u_i'(x,y,z,t) u_i'(x,y,x,t+\tau)\rangle}{u_{i_{\rm rms}}^2}, \qquad \text{no sum},$$

and pressure signals ($R_{pp}(x,y,\tau) = \langle p'(x,y,z,t)p'(x,y,z,t+\tau)\rangle / p_{\rm rms}^2$) probed at different locations inside the domain with the local root mean square fluctuation defined to normalise to one the correlation at zero time separation, e.g. $R_{ii}(x,y,0) = 1$. Here, and in the following, angular brackets will indicate averages over homogeneous coordinates, z and t,

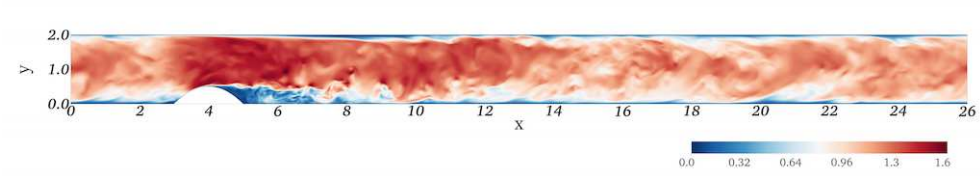

Figure 4: Instantaneous streamwise velocity contour plots in x-y plane.

while a prime indicates the fluctuation with respect to the local mean value. Some probes are located just beyond the bump (panel (a) of the figure) and some others in the fully developed channel-like flow (panel (b) of the figure). The correlations confirm that fields separated by Δt_{stat} are uncorrelated. For the same points, the spatial correlation of streamwise velocity fluctuations in the spanwise direction are shown in panel (c) of figure 3. The spatial correlation is defined as $R_{xx}(x, y, \zeta) = \langle u'_x(x, y, z, t)u'_x(x, y, z + \zeta, t)\rangle / u^2_{x_{\rm rms}}$. In figure 3c the solid line refers to the correlation just beyond the bump whilst the dashed line refers to the correlation in the fully developed channel flow. The spatial separation is normalised with (nominal) wall units $\zeta^+ = \zeta Re^0_\tau$. It is clear that in the channel-like region the minimum correlation occurs at $\zeta^+ \simeq 100$ assuring that the spanwise length is suitable to avoid confinement effects on the turbulent structures. With regards to the correlation close to the bump, the correlation minimum occurs at $\zeta^+ \simeq 80$. The inset in the figure reports the same quantities as a function of the spanwise separation normalised with the external unit.

3. Results

The first part of this section is devoted to the qualitative description of the flow with particular reference to one of the instantaneous configurations of case (C). A deeper statistical analysis is then presented to highlight the difference between the three geometries in section § 2.

3.1. *Instantaneous fields*

Figure 4 shows the instantaneous streamwise velocity field in a plane normal to the spanwise direction. The case (C) is here reported to qualitatively describe the main features of the flow. Following the flow direction, from left to right, just before the bump a thickening of the boundary layer close to the bottom wall occurs due to the adverse pressure gradient induced by the presence of the bump. In correspondence of the bump, the section decrease produces an abrupt flow acceleration, and the boundary layers at both top and bottom wall become thinner. The flow separation is clear and a thin and intense shear layer detaches from the bump in correspondence with the recirculation bubble after the bump. At the top wall, the thickening of the boundary layer is a consequence of the adverse pressure gradient present in the region just behind the bump. In the same region the velocity decreases, even though more smoothly than the previous flow acceleration. Downstream, $x > 20$, the velocity field recovers the known behaviour of the fully developed channel flow.

Figure 5 shows two dimensional xz-plane velocity magnitude contour plots at three different y positions. As anticipated in § 2, a significant length has been used in the x-direction (streamwise direction) to allow the flow to recover to channel-like behaviour. Panel (a) shows the xz-plane close to the bottom wall at $y^+ = 15$ where the empty region represents the intersection of the plane with the bump. The recirculation region

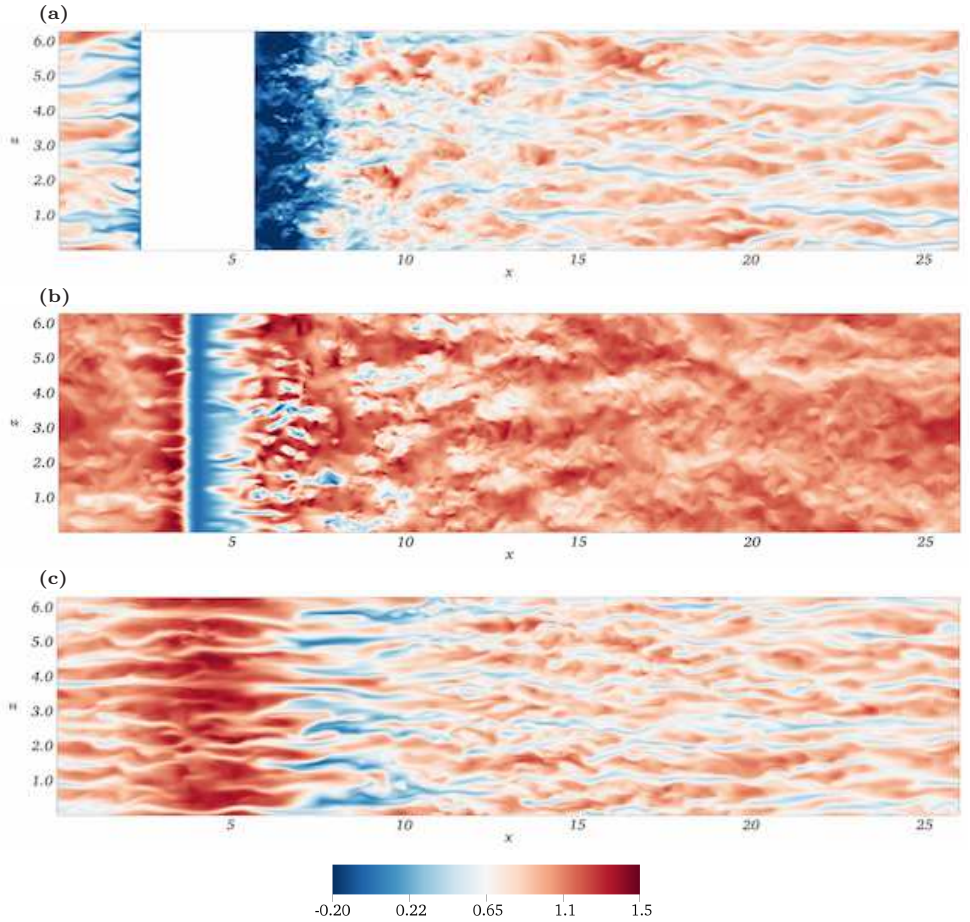

Figure 5: Instantaneous streamwise velocity contour plots in x-z planes at $y^+ = 15$ from the bottom and top walls in panel (a) and (c) respectively and at $y = 0.5$ in panel (b).

Figure 6: Instantaneous vorticity surfaces at constant magnitude.

found behind the bump is characterised, at this distance from the wall, by negative velocity and small-scale structures. Proceeding downstream, these structures tend to elongate in the flow direction and take the typical streaky shape found in a fully developed turbulent channel flow. The xz-plane of panel (b) just touches the top of the bump which is indicated by the zero velocity line (white) in the contour plot. This view allows the acceleration of the flow just before the bump and its deceleration just beyond the bump to be appreciated. Also, in this plane, the structures far away from the bump tend to

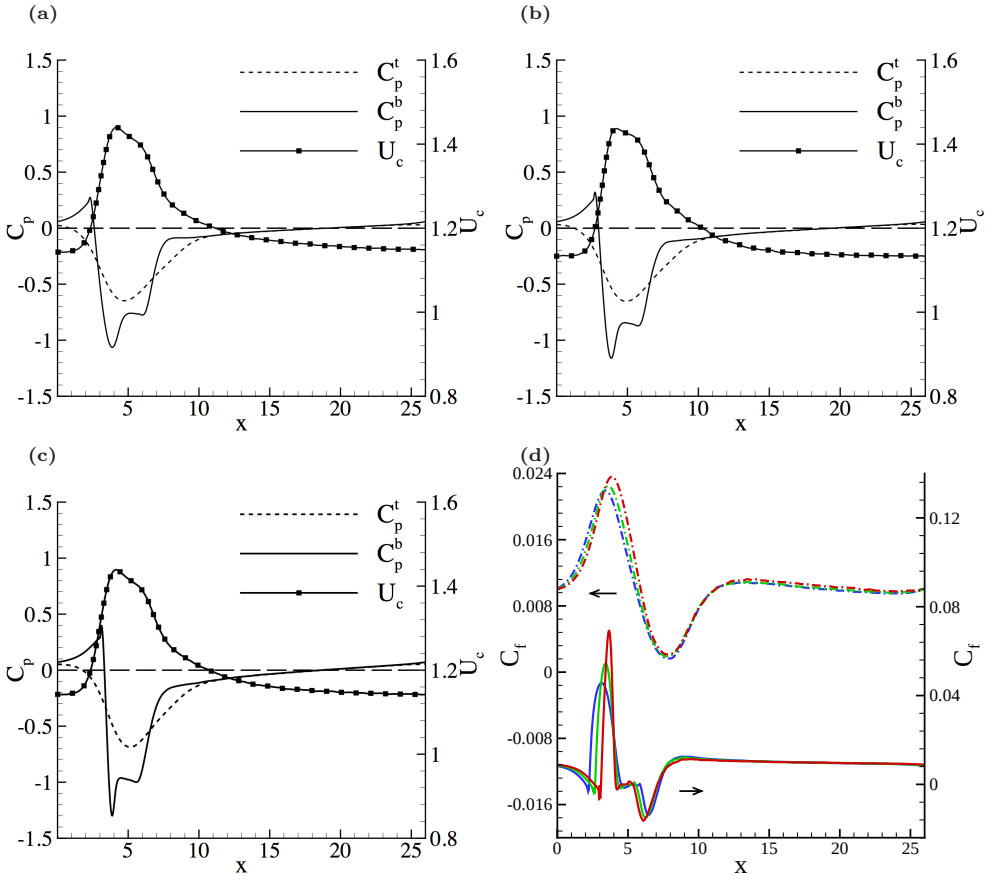

Figure 7: Mean axial profiles of the pressure coefficient at top C_p^t (dotted line) and bottom C_p^b (solid line) and of the mean axial centreline velocity (solid/symbol line). Panel (a): case (A), panel (b): case (B), panel (c): case (C). Panel (d): skin friction coefficient at the top wall (dash-dotted line, left axis) and the bottom wall (solid line, right axis). The color code is the same as in figure 2.

increase in size to finally resemble the typical structures of planar channel flow. In this case, due to the distance from the lower wall, streaks are not detected. Panel (c) shows the xz-plane close to the top wall at $y^+ = 15$ where the effect of the bump on the velocity is less evident but still present. In particular, a velocity increase is seen at the bump's location, evidently due to the cross-section restriction. This is followed by a low velocity region corresponding to where the separation bubble ends. Close to the top wall, unlike the bottom wall region, the turbulent structures seem to maintain a streamlined shape more similar to the streaks occurring in a fully developed turbulent channel flow.

Figure 6 reports the vorticity to visually detect the turbulence structures and their characteristic length scales. As anticipated, just behind the bump, small three dimensional structures filling the recirculation region in the bottom channel half are generated by the shear layer. These structures do not persist downstream where elongated structures appear close to the walls.

Case	C_d^{form}	$C_d^{friction} - C_d^{channel}$	C_d
A	$1.06 \cdot 10^{-2}$	$0.21 \cdot 10^{-2}$	$3.07 \cdot 10^{-2}$
B	$1.28 \cdot 10^{-2}$	$0.18 \cdot 10^{-2}$	$3.26 \cdot 10^{-2}$
C	$1.55 \cdot 10^{-2}$	$0.14 \cdot 10^{-2}$	$3.49 \cdot 10^{-2}$

Table 1: Form and friction contributions to the drag coefficient for the three geometries. The third column is the difference between the friction drag coefficient of the actual geometry and that of an equivalent planar channel.

3.2. *Statistical Analysis*

In the following, the average of a quantity f is denoted by a capital letter, F, and, as before, a prime is used to express fluctuations, f'. The instantaneous pressure can be decomposed as the sum of a contribution linearly decreasing in the streamwise direction, which is associated to the instantaneous pressure drop Δp across the channel, plus a departure $\tilde{p}$ from the linear law that in the following will be called modified pressure,

$$p(\mathbf{x}, t) = -\frac{\Delta p}{L_x} x + \tilde{p}(\mathbf{x}, t) \ .$$

In the present simulations $\Delta p(t)$ does not significantly fluctuate in time, within 1%, although it is in principle continuously adjusted to keep the flow rate constant. The drag coefficient in terms of the present dimensionless variables is

$$C_d = 4\frac{\Delta P}{L_x} = -\frac{2}{L_x}\int_{walls} \langle \mathbf{t} \rangle \cdot \mathbf{e}_x dl \, ,$$

where $\Delta P = \langle \Delta p \rangle$ is the average pressure drop, $\mathbf{t}$ is the (dimensionless) tension at the wall (pressure plus shear force) and $\mathbf{e}_x$ is the unit vector in the streamwise direction. The drag, at the same flow rate, is larger than in a channel flow between perfectly flat, parallel walls. As expected, it increases moving from the most streamlined (A) to the most bluff profile (C), see table 1. The drag exerted on the channel walls can be decomposed in form and friction components, namely

$$C_d^{form} = \frac{2}{L_x}\mathbf{e}_x \cdot \int_{walls} P\mathbf{n} dl \, , \qquad C_d^{friction} = -\frac{2}{L_x}\mathbf{e}_x \cdot \int_{walls} \mu \frac{\partial \mathbf{U}}{\partial n} dl \, ,$$

where $\mathbf{n}$ is the unit normal exiting the fluid domain. The form drag increases by 50% going from the most streamlined to most bluff shape. It should be noted that the friction drag coefficient for a planar channel flow at the same nominal Reynolds number could be estimated as $C_d^{channel} = 4\left(Re_\tau^0/Re_b\right)^2 = 1.80 \cdot 10^{-2}$. The table shows that most of the drag due to the presence of the bump should be interpreted as form drag. Indeed, the friction exerted on an equivalent planar channel is basically the same, $C_d^{friction} \simeq C_d^{channel}$.

The behaviour of the pressure can be used to monitor the flow near the walls. To this purpose a modified pressure coefficient has been defined in terms of the normalised average pressure departure from the linear law,

$$C_p^{t/b}(x) = 2\left\langle \tilde{p} \right\rangle\big|_{y=2/y=0} \ ,$$

where the superscripts 't' and 'b' refer to the top and bottom wall respectively. The addition of $-2x\Delta P/L_x$ recovers the standard pressure coefficient.

Figure 7 shows the modified pressure coefficient at the top and bottom wall together with the mean centreline streamwise velocity for the simulations (A), (B) and (C) in panels (a), (b) and (c) respectively. As expected, the pressure changes more abruptly near the lower wall near the bump than at the opposite wall. Approaching the bump from upstream, C_p^b initially increases leading to a small recirculation region just ahead of the bump. The pressure then decreases to a minimum located just ahead of the top of the bump. Immediately downstream, the pressure starts to rise up to the separation point, where flow detaches from the bump profile. The ensuing recirculation bubble keeps the (modified) pressure to an almost constant plateau. Beyond the bubble, the pressure rises again. If the channel length were substantially longer than could be presently afforded, the modified pressure would have vanished sufficiently far from the bump. In fact, due to a small effect of streamwise confinement the modified pressure coefficient is slightly positive. The pressure gradient at the top wall is weaker than at the bottom wall, with a minimum value just after the bump top. The top wall pressure gradient then experiences the same constant value of the bottom wall in a large region after the bump where the velocity tends to recover the fully developed profile of the turbulent channel flow. The mean flow experiences an abrupt acceleration in the first part of the bump and reaches the maximum at the bump top. The behaviour described above is generic and common to all the geometries. From the quantitative point of view, going from the streamlined to the bluff bump, from case (A) to case (C), the pressure gradients progressively increase becoming most intense for the case (C). The minimum pressure values decrease at both the bottom and top wall. No significant variations are observed for the centreline axial velocity. Panel (d) in figure 7 reports the skin friction coefficient $C_f = 2\,\tau_w$. At the bottom wall C_f is negative just behind the bump for all the three cases indicating the presence of the separation bubble. For case (C), the bluff bump, a slightly negative value of the wall shear stress is detected in front of the bump, in correspondence with a small recirculation bubble. As expected, the maximum shear stress is reached on the bump, just before its top, where the velocity increase results in a larger wall stress. The shear stress increases going from the more streamlined, case (A), to the more bluff bump shape, case (C). The skin friction at the top wall is generally smaller than at the bottom wall. No locally negative values are found, showing that the pressure gradient is mild enough to keep the flow attached to the top wall for the present geometries. Significant variations are nonetheless detected, with the maximum occurring just before the bump top and the minimum occurring at the end of the recirculation bubble at the bottom wall. Far from the bump the skin friction recovers the constant behaviour of the planar channel flows.

Figure 8 shows a contour plot of average vorticity with the mean velocity vectors for the three geometries. The only non vanishing mean vorticity component is $\langle\zeta_z\rangle = \partial_x\langle u_y\rangle - \partial_y\langle u_x\rangle$ and the mean velocity is two dimensional (streamwise, $\langle u_x\rangle$, and wall-normal, $\langle u_y\rangle$). The vorticity maxima occur near the wall where the mean velocity gradients are significantly high. The recirculation bubble just after the bump is clear from the plots, with the flow inversion highlighted by the positive vorticity peak at the bottom wall after the bump. Overall, the dynamics of the separation follows the classical path. By progressively restricting the section, the first part of the bump makes the flow accelerate and gives rise to the pressure decrease which is mechanically responsible for the acceleration of the fluid particles. After the top of the bump the area available to the flow increases again and the flow decelerates by incompressibility and mass conservation. The flow deceleration is associated with an adverse pressure gradient after the bump top that produces backwards flow near the solid wall, giving rise to flow detachment. The

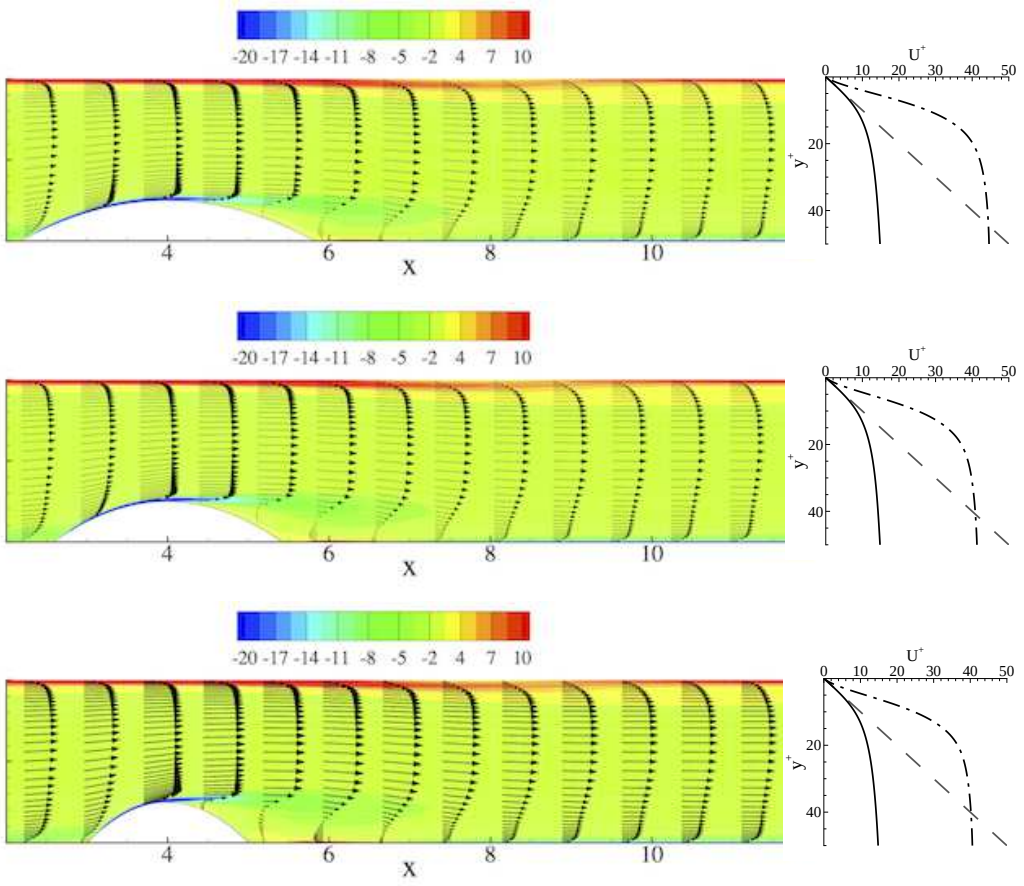

Figure 8: Left column (from top to bottom): Mean velocity (vectors) and mean vorticity (contours) for the three cases (A), (B) and (C). The domains are intentionally cut to highlight the region close to the bump. Right column: velocity profiles in the near wall region at the top of the channel, $x = 8$ (dash-dotted line) and $x = 24$ (solid line). For reference, the dashed line is $u^+ = y^+$.

recirculation bubble occurs in all three geometries and becomes larger moving from the streamlined case (A) to the more bluff geometry in case (C). More detailed information is gathered by looking at the velocity profiles in figure 9. The vorticity close to the top wall is always positive, confirming that no recirculation bubble is formed even in the region of adverse pressure gradient, see figure 7. The velocity profile in the region of adverse pressure gradient shows an inflection point extremely close to the wall that, hardly detected even in inner variables, becomes apparent in logarithmic scale (not shown). In the plots, its presence can be inferred by the tangent right at the wall, (dashed line) which systematically lies below the velocity profile (dash-dotted line).

Figure 9 shows the mean axial velocity, $\langle u_x \rangle$, (solid line) and wall-normal velocity, $\langle u_y \rangle$, (dashed line) profiles at the six streamwise stations (a) to (f) highlighted in figure 2. The effect of the bump becomes stronger going from case (A) to case (C). For the different cases, the velocity profiles far from the bump, panel (f), tend to collapse and the mean wall normal velocity to vanish. The small region with negative axial velocity, station

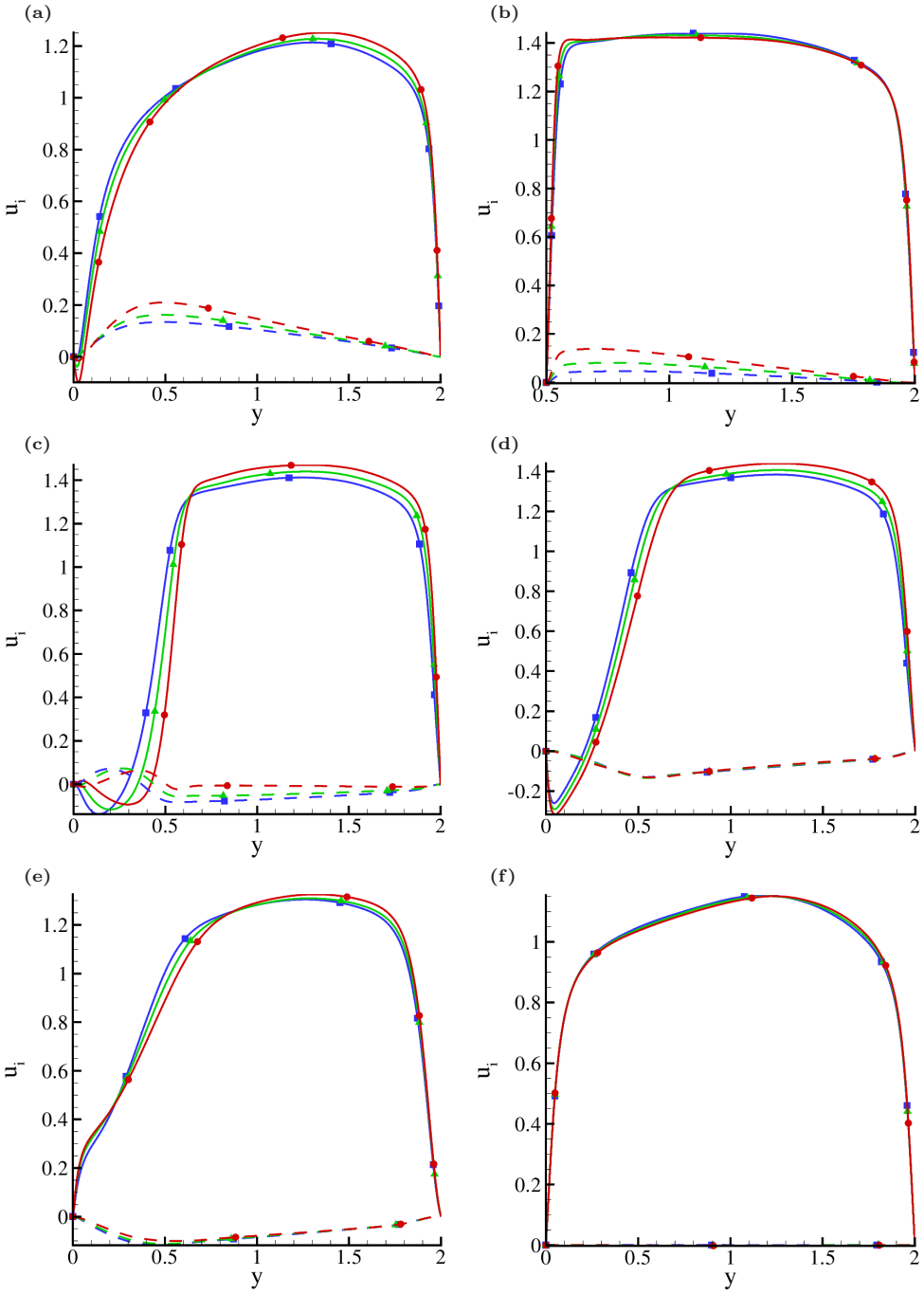

Figure 9: Mean axial velocity, $\langle u_x \rangle$, (solid line) and wall-normal velocity, $\langle u_y \rangle$, (dashed line) profiles at the six positions (a) to (f) highlighted in figure 2. The colour legend follows that of the figure 2.

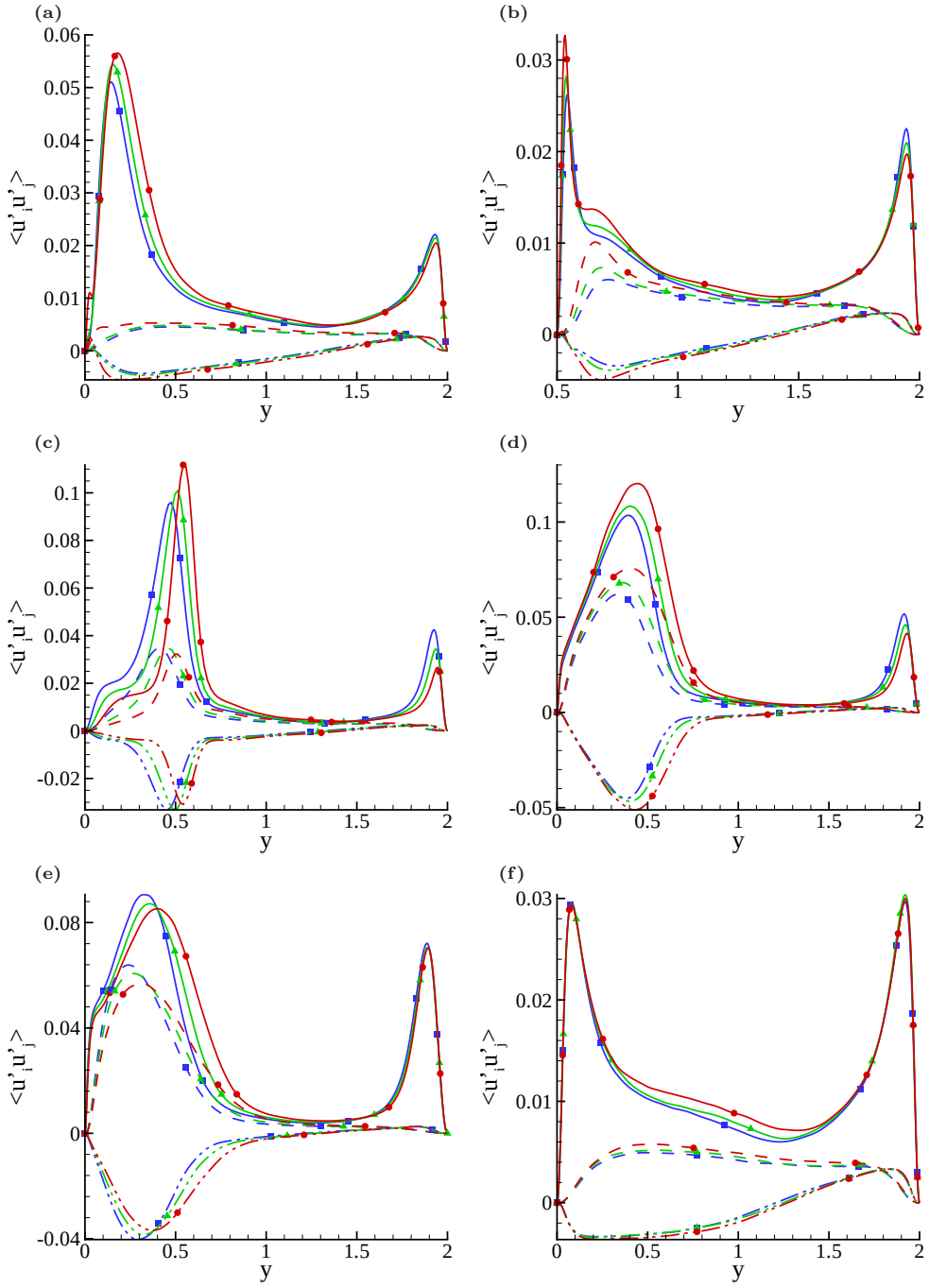

Figure 10: Mean profiles of the Reynolds stress tensor $\langle u_i' u_j' \rangle$ at different stations, see figure 2–panels (a-f) correspond to stations I-VI, respectively, as a function of the wall normal coordinate. The colours blue, green and red correspond to the cases (A), (B), and (C) respectively. $\langle u_x'^2 \rangle$: solid line, $\langle u_y'^2 \rangle$: dashed line, $\langle u_x' u_y' \rangle$: dash-double dotted line. The plot ranges change for each panel for better visualisation.

I, panel (a), corresponds to the already mentioned small recirculation bubble whose intensity and dimension increase from case (A) to case (C). Behind the bump, stations III-V, panels (c-e), case (C) produces the largest recirculation bubble, see the region interested by a negative streamwise velocity just behind the region of higher velocities in the bulk. Moving towards the more streamlined bump the progressive decrease of the recirculation bubble dimension and of the bulk mean streamline velocities is apparent.

Figure 10 shows the Reynolds stresses as a function of the wall distance. Similar to the planar channel flow, the wall-normal velocity fluctuations, $\langle u_y'^2 \rangle$, and the shear stress, $\langle u_x' u_y' \rangle$, are less intense than the streamwise fluctuations, $\langle u_x'^2 \rangle$. The recirculation bubble produces a significant increase in stresses which are up to one order of magnitude larger compared to those downstream, see panels (c-e) corresponding to sections III-V respectively. The trend is similar for the three geometries but quantitative differences appear. Case (A) (blue line) always produces the smallest fluctuations intensity close to the bottom wall and the largest fluctuations intensity close to the top wall, see panels (a-d). The opposite behaviour is observed for case (C). Panels (c-e) show that, going from case (A) to case (C), the fluctuation peak close to the bottom wall tends to move towards the channel centre indicating the growth of the recirculation bubble. The increase in fluctuations in the shear layer has strong effects on the turbulent kinetic energy production, as will be discussed in § 3.3.

3.3. *Kinetic Energy Balance*

The Reynolds decomposition entails the splitting of the total kinetic energy in two parts, $K = K_M + k_T$, namely $K_M = 1/2 \, \langle u_i \rangle \langle u_i \rangle$ and $k_T = 1/2 \langle u_i' u_i' \rangle$. In the literature, little attention is typically paid to the kinetic energy of the mean field K_M and most interest is focused on the turbulent contribution k_T, due to the usually simple flow configuration. In the present case, due to the complexity of the flow, the mean field is non trivial and both components of the kinetic energy are worth being investigated in detail.

Under statistically stationary conditions, the mean flow kinetic energy equation reads

$$\frac{\partial \Phi_{Mj}}{\partial x_j} = -\varepsilon_M - \Pi + \frac{\Delta P}{L_x} U_x \,, \tag{3.1}$$

where $\varepsilon_M = 1/Re (\partial U_i / \partial x_j)(\partial U_i / \partial x_j)$ is the mean flow energy dissipation and $\Pi = -\langle u_i' u_j' \rangle \partial U_i / \partial x_j$ is the turbulent kinetic energy production. $U_x \Delta P / L_x$ is the average power input to the system. Although this term could have been written as the divergence of a flux, it is here isolated from the spatial flux of mean flow energy Φ_{Mj},

$$\Phi_{Mj} = U_j K_M + U_j \langle \tilde{p} \rangle - \frac{1}{Re} \frac{\partial K_M}{\partial x_j} + U_i \langle u_i' u_j' \rangle \,, \tag{3.2}$$

which only redistributes energy among different regions of the flow, providing zero net power when integrated over the entire flow domain. In particular for a planar channel flow $\partial \Phi_{Mj} / \partial x_j$ vanishes altogether.

Panel (a) in figure 11 shows the different terms of equation (3.1) normalised with the total average power injected in the mean flow per unit volume, $\left(Q \Delta P + \langle Q' \Delta p' \rangle \right) / V$ where Q is the mean flow rate, Q' its fluctuation and V the volume of the flow domain. For the reader's convenience, it is worth recalling that, in figure 11, the flux is also normalised by the same dimensionless energy input, $\Phi_{Mj} V / (Q \Delta P + \langle Q' \Delta p' \rangle)$, since the nominal channel half is normilised to one. Clearly, the overall power injected in the system, $Q \Delta P + \langle Q' \Delta p' \rangle$ is balanced by the total dissipation rate, $\int (\varepsilon_M + \varepsilon_T) \, dV$. Most energy is introduced by the forcing $\Delta P / L_x$ in the regions where U_x is highest, namely at the centre of the channel, in particular at the restriction where the flow is accelerated,

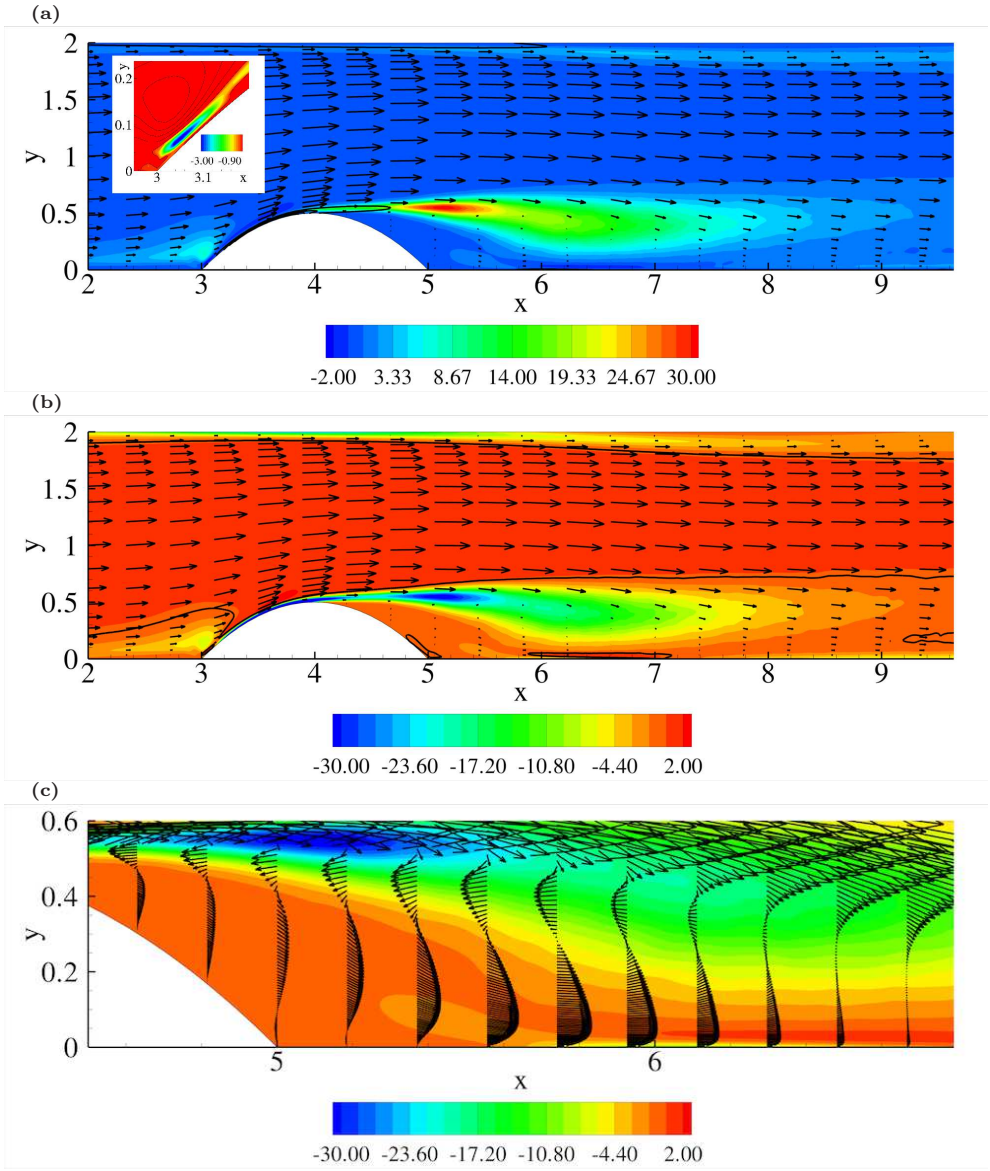

Figure 11: Panel (a), turbulent kinetic energy production, $\Pi V/(Q\Delta P + \langle \Delta P' Q' \rangle)$, (coloured contours); mean flow spatial energy flux, Φ_{Mj}, (vectors); mean flow dissipation rate, $\varepsilon_M V/(Q\Delta P + \langle \Delta P' Q' \rangle)$, (black isolines). Inset of panel (a), magnification of the forepart of the bump, where negative turbulent kinetic energy production occurs (the colour legend is intentionally changed). Panel (b), divergence of the mean flow spatial energy flux $V\partial\Phi_{Mj}/\partial x_j (Q\Delta P + \langle \Delta P' Q' \rangle)$ (coloured contours) superimposed to the vector field $\Phi_{Mj} V/(Q\Delta P + \langle \Delta P' Q' \rangle)$. The thick solid line is the zero isoline of the divergence. Panel (c), magnification of the region just behind the bump, same data as in panel (b). All data refer to case (C).

see figure 9. The turbulent kinetic energy production is positive almost everywhere in the field, except in the forepart of the bump, see the enlargement in panel (a) of figure 11. Most turbulence production occurs in the shear layer. The mean flow dissipation rate, ε_M, is especially intense near the walls, particularly where strong velocity gradients occur at the front of the bump, at the detaching shear layer and at the opposite wall in correspondence with the separation bubble. The mean flow energy is captured by the flux Φ_{Mj} where its divergence is positive and released where it is negative, see panel (b). The comparison with panel (a) shows that the flux substantially contributes in feeding the turbulent kinetic energy production and the dissipation rate. The flux is sustained by the forcing which, although small, is distributed all over the domain, being larger in the centre of the channel. A detail of the region just behind the bump is shown in panel (c). The mean flow kinetic energy balance for cases (A), (B) and (C) is reported in figure 12. The bluff shape (C) transfers a larger percentage of the power injected in the mean flow into the fluctuations. Accordingly, the fluctuation level is the highest, figure 10.

The balance equation for the turbulent kinetic energy reads

$$\frac{\partial \Phi_{Tj}}{\partial x_j} = -\varepsilon_T + \Pi + \langle \frac{\Delta p'}{L_x}\, u_x' \rangle \,, \tag{3.3}$$

where $\varepsilon_T = \langle \partial u_i'/\partial x_j \, \partial u_i'/\partial x_j \rangle / Re$ is the turbulent kinetic energy dissipation rate, Π is the production as in equation (3.1), and $\langle \Delta p' \, u_x'/L_x \rangle$ is the source of fluctuating energy. Φ_T is the spatial flux,

$$\Phi_{Tj} = U_j k_T + \frac{1}{2}\langle u_i' u_i' u_j' \rangle + \langle \tilde{p}' u_j' \rangle - \frac{1}{Re}\frac{\partial k_T}{\partial x_j} \,, \tag{3.4}$$

which contributes zero net power when integrated over the whole domain. $\langle \Delta p' \, u_x'/L_x \rangle$ provides a negligible amount of energy, typically less than 1%, implying that, as expected, turbulent fluctuations are sustained by the production term.

Figure 13 addresses the balance of turbulent kinetic energy. The production term, panel (a), injects energy to the fluctuations mainly in the shear layer behind the bump. Part of the energy is locally dissipated, ε_T. The remainder, $\Pi > \varepsilon_T$, corresponding to the majority of the available energy, feeds the flux whose divergence is positive in the same region, panel (b). The flux moves the energy away to release it where the divergence is negative, $\Pi < \varepsilon_T$, typically in the bulk of the recirculation bubble and near the wall. A detail of the region just behind the bump is shown in panel (c). Further downstream, where the flow recovers the behaviour of a planar channel flow, the flux is fed at the buffer layer to be released and dissipated partly at the wall and partly in the bulk of the flow. Close to the top wall, in the region corresponding to the adverse pressure gradient, production is also locally dominant, $\partial \Phi_{Tj}/\partial x_j > 0$. Moving from the most streamlined to bluffest geometry, although the qualitative behaviour in figure 14 remains basically the same, the production increases substantially, by almost 50%.

4. Conclusions

The dynamics of a turbulent separation bubble was analysed by Direct Numerical Simulations (DNS) of channel flows with a bump at one of the walls. The resulting composite flow includes three physically different situations: i) the separation bubble behind the bump; ii) the attached boundary layer with adverse pressure gradient at the opposite wall; iii) the classical turbulent flow in the planar channel downstream. The simulations are based on the spectral element method, as implemented in the Nek5000 code (Fischer *et al.* 2008). Beside addressing the global features of the flow, such as

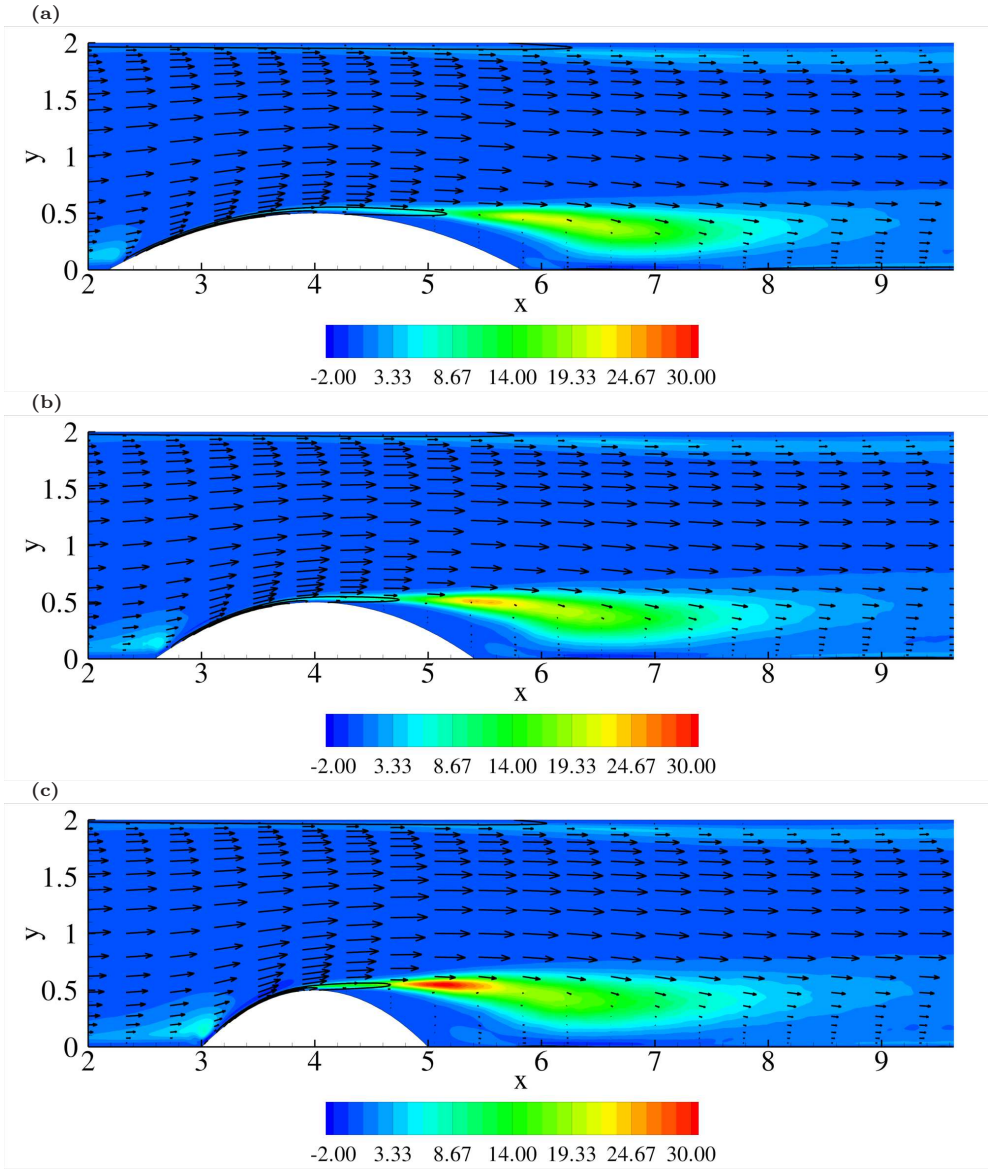

Figure 12: Mean kinetic energy balance equation: turbulent kinetic energy production (background coloured contour plot), mean energy dissipation (solid isolines) and mean energy spatial flux (vectors). The three simulations, (A), (B) and (C), are shown from top to bottom respectively.

pressure and wall shear stress distributions, mean profiles and turbulent fluctuations, the main results concern the detailed analysis of the mechanisms of energy production, dissipation and transfer for both the mean and the fluctuating fields, which were not fully addressed yet in the literature, and which are not trivial given the spatial complexity of the flow.

The separation behind the bump generates small scale structures which grow downstream, recovering the classical behaviour found in the planar turbulent channel flow.

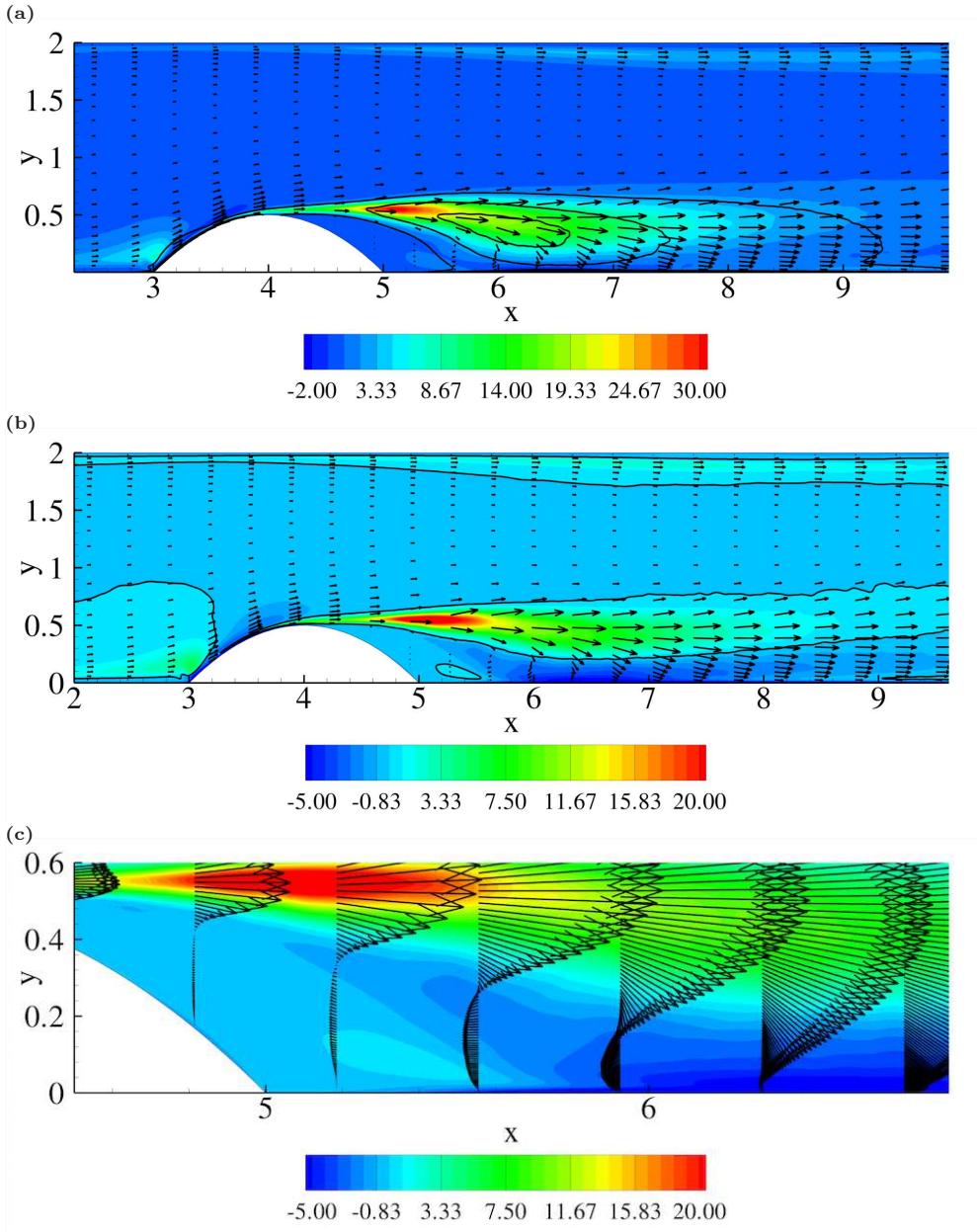

Figure 13: Panel (a), turbulent kinetic energy production, $\Pi\, V/(Q\Delta P + \langle Q'\Delta p'\rangle)$, (coloured contours); spatial energy flux associated with the velocity fluctuations, Φ_{Tj}, (vectors); velocity fluctuation dissipation rate, $\varepsilon_T\, V/(Q\Delta P + \langle Q'\Delta p'\rangle)$, (black isolines). Panel (b), divergence of the mean flow spatial energy flux $\partial\Phi_{Tj}/\partial x_j\, V/(Q\Delta P + \langle Q'\Delta p'\rangle)$ (coloured contours) superimposed to the vector field $\Phi_{Tj}\, V/(Q\Delta P + \langle Q'\Delta p'\rangle)$. The thick solid line is the zero isoline of the divergence. Panel (c), magnification of the region just behind the bump, same data as in panel (b). All data refer to case (C).

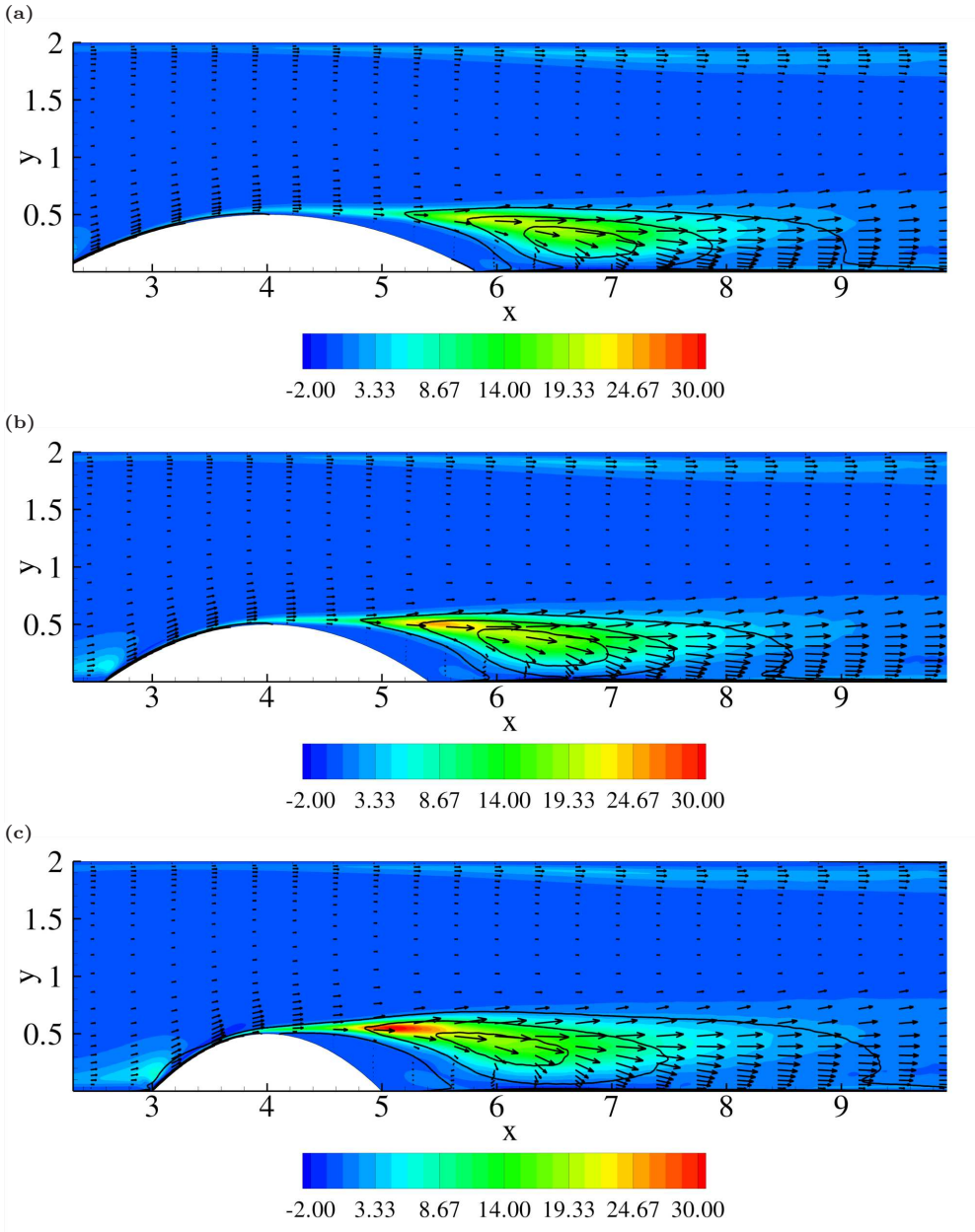

Figure 14: Turbulent kinetic energy balance equation: turbulent kinetic energy production (background coloured contour plot), turbulent energy dissipation (solid isolines) and turbulent energy spatial flux (vectors). The three simulations, (A), (B) and (C), are shown from top to bottom respectively.

The most evident effect of the geometry is right behind the bump, where, from the streamlined to the bluff geometry, the recirculating region increases in size. Even though the separated region width changes with geometry, the position where it ends is always constant. This suggests that the position of the reattachment point is mainly correlated with the height of the bump itself. Consequently, the width of the recirculation bubble is

inversely proportional to the width of the bump. This gives rise to the strong form drag that is experienced by the bump, which increases with the bluffness. The change in the friction component of drag with respect to the classical channel flow, is comparatively less significant. A substantial interaction occurs also with the opposite wall where, just behind the bump, a significant adverse pressure gradient is induced in correspondence with the recirculation region.

The mean flow provides almost entirely the energy for sustaining the turbulence. A region in front of the bump exists, however, where production becomes negative, indicating a reverse transfer of energy from the fluctuating to the mean flow. Due to the presence of strong gradients near the solid walls and in the shear layer, the amount of energy dissipated in the mean flow is not negligible. The mean flow draws energy from the external forcing, in the present case from the pressure drop applied throughout the channel, in the bulk of the flow where the velocity is largest. The corresponding energy flux moves this energy to the regions where it is either directly dissipated or intercepted in the shear layer by the production term which sustains the fluctuations. A strong peak of turbulent kinetic energy production is indeed localised in the shear layer separating the bubble from the external flow. Part of the turbulent kinetic energy produced at the shear layer feeds the turbulent fluctuations inside the bubble to be dissipated at the bottom wall, in the region just behind the bump. The more bluff geometry captures more energy as to feed the more intense velocity fluctuations in the recirculation. The remaining part of produced energy is transported away from the bump by the turbulent kinetic energy flux, to contribute feeding the core of the flow downstream. Progressively, the different terms of the budget recover the known profiles of a classical channel flow, with production peaking in the buffer layer.

In conclusion, the present results shed light on the intermingled processes of production, transfer and dissipation of energy in complex turbulent flows where a crucial role is played by the flux terms that move the energy from places where it is generated to the locations where most dissipation occurs. An issue still to be explored concerns the scale distribution of the energy involved in the different processes sustaining the fluctuations in the separation region, which calls for a generalised form of scale by scale energy budget, as recently exploited for the simpler case of the planar channel flow (Cimarelli *et al.* 2013).

The research leading to these results has received funding from the European Research Council under the ERC Grant Agreement no. 339446. PRACE, under grant no. 2014112647, has awarded access to resource FERMI based in Bologna, Italy.

REFERENCES

Bai, H. L., Zhou, Y., Zhang, W. G., Xu, S. J., Wang, Y. & Antonia, R. A. 2014 Active control of a turbulent boundary layer based on local surface perturbation. *Journal of Fluid Mechanics* .

Chong, M.S., Soria, J., Perry, A. E., Chacin, J., Cantwell, B. J. & Na, Y. 1998 Turbulence structures of wall-bounded shear flows found using dns data. *Journal of Fluid Mechanics* **357**, 225–247.

Cimarelli, A., Angelis, E. De & Casciola, C. M. 2013 Paths of energy in turbulent channel flows. *Journal of Fluid Mechanics* **715**.

Dengel, P. & Fernholz, H.H. 1990 An experimental investigation of an incompressible turbulent boundary layer in the vicinity of separation. *Journal of Fluid Mechanics* **212**, 615–636.

Fischer, P., Lottes, J. W. & Kerkemeier, S. G. 2008 Nek5000 - open source spectral element cfd solver.

Krogstad, P. A. & Skaare, P. E. 1995 Influence of the strong adverse pressure gradient on the turbulent structure in a boundary layer. *Physics of Fluids* **7** (8), 2014–2024.

Marquillie, M. & Ehrenstein, U. W. E. 2003 On the onset of nonlinear oscillations in a separating boundary-layer flow. *Journal of Fluid Mechanics* **490**, 169–188.

Marquillie, M., Laval, J-P. & Dolganov, R. 2008 Direct numerical simulation of a separated channel flow with a smooth profile. *Journal of Turbulence* (9).

Marusic, I., Talluru, K. M. & Hutchins, N. 2014 Controlling the large- scale motions in a turbulent boundary layer. *Fluid-Structure- Sound Interactions and Control* .

Na, Y. & Moin, P. 1998*a* Direct numerical simulation of a separated turbulent boundary layer. *Journal of Fluid Mechanics* **374**, 379–405.

Na, Y. & Moin, P. 1998*b* The structure of wall-pressure fluctuations in turbulent boundary layers with adverse pressure gradient and separation. *Journal of Fluid Mechanics* **377**, 347–373.

Neumann, J. & Wengle, H. 2004 Coherent structures in controlled separated flow over sharp-edged and rounded steps. *Journal of Turbulence* **5** (22), 14.

Ohlsson, Johan, Schlatter, Philipp, Fischer, Paul F & Henningson, Dan S 2010 Direct numerical simulation of separated flow in a three-dimensional diffuser. *Journal of Fluid Mechanics* **650**, 307–318.

Patera, A. T. 1984 A spectral element method for fluid dynamics. *Journal of Computational Physics* **54**, 468–488.

Simpson, R.L. 1989 Turbulent boundary-layer separation. *Annual Review of Fluid Mechanics* .

Skaare, P. E. & Krogstad, P. A. 1994 A turbulent equilibrium boundary layer near separation. *Journal of Fluid Mechanics* **272**, 319–348.

Skote, M. & Henningson, D. S. 2002 Direct numerical simulation of separating turbulent boundary layer. *Journal of Fluid Mechanics* pp. 107–136.

Spalart, P. R. 1988 Direct simulation of a turbulent boundary layer up to r θ= 1410. *Journal of Fluid Mechanics* **187**, 61–98.

Spalart, P. R. & Watmuff, J. H. 1993 Experimental and numerical investigation of a turbulent boundary layer with pressure gradients. *Journal of Fluid Mechanics* **249**, 337–371.

Webster, D. R., DeGraaff, D. B. & Eaton, J.K. 1996 Turbulence characteristics of a boundary layer over a two-dimensional bump. *Journal of Fluid Mechanics* **320**, 53–69.

Wilcox, D. C. 1993 Turbulence modeling for cfd. *DCW Industries Inc.* .

Wu, X. & Squires, K. D. 1998 Numerical investigation of the turbulent boundary layer over a bump. *Journal of Fluid Mechanics* **362**, 229–271.